Macromolecules **2005,** *38,* 3395−3405

In-Situ Grazing Incidence Small-Angle X-ray Scattering Studies on Nanopore Evolution in Low-*k* Organosilicate Dielectric Thin Films

Byeongdu Lee,[†] Jinhwan Yoon,[†] Weontae Oh,[†] Yongtaek Hwang, Kyuyoung Heo, Kyeong Sik Jin, Jehan Kim, Kwang-Woo Kim, and Moonhor Ree*

Department of Chemistry, Pohang Accelerator Laboratory, Center for Integrated Molecular Systems, Polymer Research Institute, and Division of Molecular of Life Sciences, Pohang University of Science and Technology, Pohang 790-784, Republic of Korea

Received September 1, 2004; Revised Manuscript Received January 18, 2005

ABSTRACT: The first in-situ two-dimensional grazing incidence small-angle X-ray scattering (2D GISAXS) study on the evolution of nanopores during the thin film formation of porous dielectrics from composite films is reported. A soluble poly(methylsilsesquioxane) (PMSSQ) precursor and a four-armed poly(ϵ-caprolactone) (PCL4) were chosen as the model matrix and porogen components within the composite film. The measured 2D GISAXS data were analyzed quantitatively using a GISAXS formula derived under the distorted wave Born approximation. It is shown that in-situ GISAXS is a powerful tool for monitoring the evolution of nanopores in dielectric thin films, providing structural characteristics such as size, size distribution, shape, electron density, and porosity, all as a function of temperature and time. In addition, the mechanism for forming imprinted nanopores in the dielectric films by sacrificial thermal degradation of the porogen was determined by in-situ GISAXS analysis. Phase separation of the PCL4 porogen was induced below 200 °C by cross-linking of the PMSSQ precursor matrix during thermal curing. This process generated porogen aggregates, each individually imprinted pore in the film through thermal degradation; the shape, size, and size distribution of the porogen aggregates are directly reflected in the dimensions of the imprinted pores. Moreover, it was found that higher porogen loadings caused larger porogen aggregates with a greater size distribution. The present results thus show that the structural characteristics of nanopores imprinted within PMSSQ dielectric films are governed by the PCL4 porogen aggregates formed through curing of the PMSSQ precursor matrix.

Introduction

Porous organosilicate materials have recently attracted much interest due to their potential applications as low dielectric constant (low-*k*) interdielectrics,[1−10] chemical and biosensor membranes,[11] catalyst supports,[12] and gas separation membranes.[13] One major route for producing porous organosilicates is the templated sol−gel synthesis of silane derivatives in the presence of labile porogens such as organic surfactants and polymers. Subsequent removal of the porogen templates generates pores in the resultant organosilicates.

In particular, much effort has been directed toward the development of low-*k* porous organosilicate dielectric thin films via the templated polycondensation of their soluble precursors in the presence of a thermally labile, organic polymeric porogen (e.g., linear copolymers,[3−6] dendritic star-shaped polymers,[7−9] and hyperbranched polymers[9,10]). Pores are subsequently formed in the resulting dielectrics through the sacrificial thermal decomposition of the porogens in the range 350−400 °C. However, the tendency of porogens to aggregate in organosilicates has limited the ability to reduce the pore size and porosity of the resulting dielectrics,[3−10] making them unsuitable for use in advanced integrated circuits (ICs) patterned with small feature sizes. In the case of dendritic star-shaped porogens, the large number of arms was found to result in severe aggregation, even with a 10 wt % porogen loading, generating both large-sized and interconnected pores in the dielectric thin films.[8,9] Thus, the development of advanced ICs requires a method to generate dielectric materials containing a uniform distribution of closed pores, with dimensions significantly smaller than the feature size. Moreover, the ability to characterize the pore structure in porous dielectric thin films is as important as developing the dielectrics and porogens themselves.

The pore structure in porous dielectric thin films has been characterized by several techniques: X-ray and neutron reflectivity,[4,5] transmission electron microscopy (TEM),[5] gas adsorption porosimetry,[1] ellipsometric porosimetry,[1,2] and positron annihilation lifetime spectroscopy.[4,9] In fact, the formation of porous films from an organosilicate precursor polymer/porogen composite is a complex procedure since the matrix precursor readily undergoes cross-linking while the porogen undergoes thermal degradation. To understand the structure of pores in the porous film, it is necessary to investigate their generation during the porous dielectric film process. Pore structure evolution during porous film process has rarely been investigated.[6]

Recently, transmission small-angle X-ray scattering (TSAXS) has emerged as a powerful technique for characterizing pore size and size distribution in porous dielectric thin films.[3] However, TSAXS requires an intense, high-energy (ca. 15 keV) X-ray beam to obtain an acceptable scattering signal, since the X-rays must be transmitted through both the dielectric film and the much thicker substrate on which the film is deposited.[3] In addition, for TSAXS to be effective, the substrate should be free of crystal domain boundaries, as these can give rise to unfavorable X-ray scattering and reflec-

---

[†] These authors contributed equally to this work.

* To whom correspondence should be addressed: e-mail ree@postech.edu; Tel +82-54-279-2120; Fax +82-54-279-3399.

10.1021/ma048214e CCC: $30.25

Scheme 1. Procedure for Preparing Nanoporous Organosilicate Thin Films from a Curable PMSSQ Precursor and a Thermally Labile, Four-Armed PCL4 Porogen

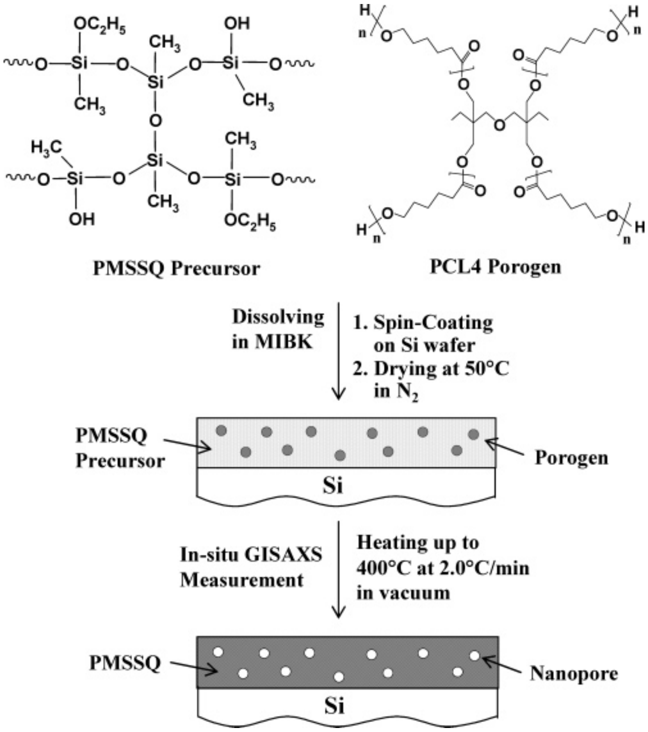

tion. Transmission small-angle neutron scattering (TSANS), on the other hand, is a powerful alternative. However, this technique requires a stack of several tens of silicon substrates, each deposited with a low-*k* dielectric thin film in order to achieve an appreciable scattering signal.[4,6,9] On the contrary, grazing incidence SAXS (GISAXS) has several important advantages over TSAXS and TSANS:[14] (i) a highly intense scattering pattern is always obtained, even for films of nanoscale thickness, because the X-ray beam path length through the film plane is sufficiently long; (ii) there is no unfavorable scattering from the substrate on which the film is coated; and (iii) easy sample preparation.

In this study, we present the first in-situ GISAXS study of the evolution of nanopores during porous dielectric film formation in a composite film containing an organosilicate precursor and a star-shaped porogen in various compositions. A soluble poly(methylsilsesquioxane) (PMSSQ) precursor and a four-armed poly(ϵ-caprolactone) (PCL4) were chosen as the model matrix and porogen components, respectively (Scheme 1). Using a synchrotron X-ray source, in-situ GISAXS measurements were carried out during thermal treatment of the PMSSQ/porogen composite films to 400 °C in a vacuum and continued during the subsequent cooling of the resulting porous films (Scheme 2). In addition, thermogravimetric analysis (TGA) and TEM measurements were performed. Detailed analyses of the measured two-dimensional (2D) GISAXS data were accomplished using a GISAXS formula derived under the distorted wave Born approximation (DWBA). The following structural characteristics of both the composite films and resulting porous films—miscibility of precursor matrix and porogen, phase separation, pore generation mechanism, pore size and size distribution, film electron density, and film porosity—were also determined.

Scheme 2. Geometry of Grazing Incidence Small-Angle X-ray Scattering (GISAXS)[a]

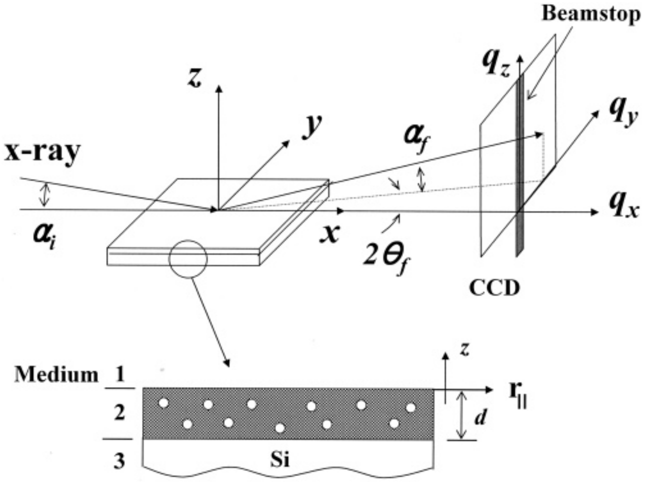

[a] An incident X-ray beam impinges on the surface of a thin film at an angle α_i, and then the scattered pattern is measured on a two-dimensional charge-coupled detector (2-D CCD), where α_f is the exit angle with respect to the film surface and $2\theta_f$ is the scattering angle with respect to the plane of incidence. A schematic structural diagram of a nanoporous dielectric film deposited onto a silicon substrate: medium 1, vacuum; medium 2, porous dielectric film; medium 3, silicon substrate. d is the thickness of medium 2 (i.e., the porous dielectric film).

Experimental Section

Materials and Sample Preparation. A soluble PMSSQ precursor containing ethoxy and hydroxyl groups (10000 $\overline{M}_w$: weight-average molecular weight) was supplied by Techneglas Co. (Perrysburg, OH).[15] ϵ-Caprolactone (CL) was dried over calcium hydride and distilled under reduced pressure; di(trimethylolpropane) was recrystallized from acetone and then dried for 24 h at 30 °C under reduced pressure. All solvents were purified under a nitrogen atmosphere with the usual methods. PCL4 porogen (6800 $\overline{M}_w$ with a polydispersity index (PDI) of 1.10 and an average degree of polymerization per arm of 8.9) was synthesized by the di(trimethylolpropane)-initiated polymerization of CL, catalyzed by stannous 2-ethylhexanoate, according to a previously reported method.[7−9,16] A series of homogeneous PCL4 porogen solutions combined with the PMSSQ precursor in methyl isobutyl ketone (MIBK) (5 wt % solid) were prepared using porogen compositions of 10, 20, 30, and 40 wt %. Each solution was filtered using a PTFE-membrane microfilter of pore size 0.20 μm, spin-coated onto the precleaned silicon [Si(100)] wafer substrates at 3000 rpm for 30 s, and then dried at 50 °C for 6 h under a nitrogen atmosphere (Scheme 1). The dried film thickness was determined using spectroscopic ellipsometry in the range 90−110 nm. The silicon substrates were precleaned as follows: (1) sonication in chloroform for 30 min; (2) sonication in a mixture of 2-propanol and deionized water (1:1 in volume) for 10 min; (3) rinsing with deionized water; and (4) drying by blowing with nitrogen.

Measurements. In-situ GISAXS measurements (as shown in Scheme 2) were conducted at the 4C1 Beamline of the Pohang Accelerator Laboratory,[17] using an X-ray source $\lambda = 0.1608$ nm, at sample-to-detector distances of 838 and 3240 mm. An X-ray incidence angle of 0.20° was used since it falls between the critical angles of the dielectric films and Si(100) substrate. Images were obtained using a two-dimensional charge-coupled detector (2D CCD) (Roper Scientific, Trenton, NJ). A set of aluminum foil strips was employed as a semitransparent beam stop. The dried films were heated to 400 °C at a rate of 2.0 °C/min and maintained at that temperature for 30 min under vacuum. Thereafter, the films were cooled to room temperature at a rate of 2.0 °C/min under

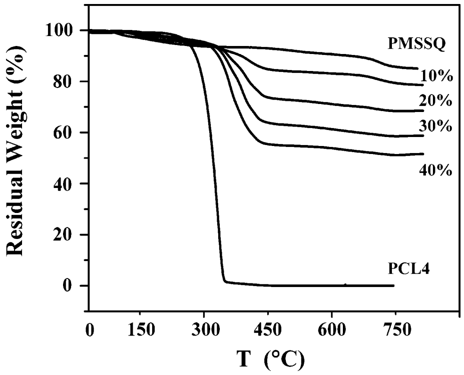

Figure 1. TGA thermograms of the PMSSQ precursor, the PCL4 porogen, and composites of the two components in various compositions. The measurements were carried out at a heating rate of 2.0 °C/min under a nitrogen atmosphere.

vacuum (see Scheme 1). Each measurement was collected for 90−140 s. In addition, the PMSSQ precursor, the dried composite samples, and porogen were examined by TGA under a nitrogen atmosphere using a TG/DT analyzer (model: EXSTAR 6000, Seiko Instruments, Japan), where a heating rate of 2.0 °C/min was adopted in order to replicate the conditions used during GISAXS measurements. TGA data were obtained while heating from 30 to 800 °C. Ellipsometric measurements were performed using a spectroscopic ellipsometer (model VASE, Woollam, Lincoln, NE). TEM measurements were carried out on samples prepared on carbon grids of 400 mesh by dip-coating in dilute solutions (1.0 wt % solid content) using an FEI microscope (model Philips CM200, Hillsboro, OR).

Theory of GISAXS and Data Analysis. In the case of porous dielectric films coated on silicon substrates produced in our study, their structure can be depicted as in the structural diagram of Scheme 2. The porous films produced in our study were found to have a surface roughness of a few angstroms,[18] which is much smaller than the film thickness of 90−100 nm; namely, the volume of interfaces to air and the silicon substrate is much smaller than that of the porous film. Taking these facts into account, the perturbation of the scattering due to interfacial roughness is reasonably small for the porous films coated on silicon substrates. Therefore, the roughness of the interfaces between the layers is not considered. Adopting the DWBA,[19−22] the scattering potential V of such porous dielectric film can be written as the superposition of two terms:

$$V = V_1 + V_2 \tag{1}$$

where V_1 is the scattering potential of a thin film without pores on a thick substrate with flat interfaces and V_2 is that of the pores in the film, which is very small compared to V_1 and can be treated as its perturbation. The only condition that must be satisfied by a division of the scattering potential is that the following wave equation should be solvable exactly:

$$(\nabla^2 + {k_0}^2 - V_1)\Psi = 0 \tag{2}$$

where Ψ is the amplitude of the scattered wave and k_0 is the modulus of the wave vector. The perturbation V_2 can be expressed in terms of the basis formed by the solutions of eq 2 as follows:

$$\Psi_{\mathrm{sc}}(\mathbf{r}) = -\frac{\mathrm{e}^{ik_0r}}{4\pi r}\int \mathrm{d}^3r'\ \Psi^1(\mathbf{r}',-\mathbf{k}_{\mathrm{f}})\ V_2(\mathbf{r}')\ \Psi^1(\mathbf{r}',\mathbf{k}_{\mathrm{i}}) \tag{3}$$

where $\Psi_{\mathrm{sc}}(\mathbf{r})$ is the amplitude of the scattered wave and $\Psi^1(\mathbf{r}')$ is the exact solution of eq 2. The incident wave is described by the wave vector $\mathbf{k}_{\mathrm{i}}$ and the scattered wave by $\mathbf{k}_{\mathrm{f}}$ (Scheme 2).

The exact solution for the unperturbed system can be obtained using the Parratt formalism.[23] For a thin film sample consisting of three layers (layers j = 1, 2, 3), as shown in Scheme 2, the refractive index n_j of layer j is $n_j = 1 - \delta_j + i\beta_j$ with a dispersion δ_j and an absorption β_j. The Fresnel reflection and transmission coefficients for each sharp interface are $r_{j,j+1} = (k_{z,j} - k_{z,j+1})/(k_{z,j} + k_{z,j+1})$ and $t_{j,j+1} = 2k_{z,j}/(k_{z,j} + k_{z,j+1})$, respectively. Here $k_{z,j}$ is the z-component of the wave vector in medium j, which is determined by the law of refraction: $k_{z,j} = k_{\mathrm{i}}\sqrt{{n_j}^2 - \cos^2\alpha_{\mathrm{i}}}$. α_{i} is the glancing angle of incidence, $k_{\mathrm{i}} = -2\pi/\lambda = -k_0$, where λ is the wavelength of the X-ray beam.

The ratio X_j of the amplitudes R_j and T_j of the outgoing and incoming electromagnetic waves in layer j, which lies between z_{j+1} and z_j (layer thickness $d_j = z_{j+1} - z_j$), can be calculated using the following recurrence relation:[18,19]

$$X_j = \frac{R_j}{T_j} = \mathrm{e}^{-2ik_{z,j}z_j}\frac{r_{j,j+1} + X_{j+1}\mathrm{e}^{2ik_{z,j}z_j}}{1 + r_{j,j+1}X_{j+1}\mathrm{e}^{2ik_{z,j+1}z_j}} \tag{4}$$

$$R_{j+1} = \frac{1}{t_{j+1,j}}\{T_jr_{j+1,j}\mathrm{e}^{-i(k_{z,j+1}+k_z)zj} + R_j\mathrm{e}^{-i(k_{z,j+1}-k_{z,j})z_j}\} \tag{5}$$

and

$$T_{j+1} = \frac{1}{t_{j+1,j}}\{T_j\mathrm{e}^{i(k_{z,j+1}-k_{z,j})z_j} + R_jr_{j+1,j}\mathrm{e}^{i(k_{z,j+1}+k_{z,j})z_j}\} \tag{6}$$

Because a semiinfinite substrate is assumed, $R_4 = 0$ and the amplitude of the incoming X-ray wave is set to $T_1 = 1$.

The solutions for the X-ray wave in the unperturbed system are as follows:

$$\Psi_1^1(\mathbf{r}) = \mathrm{e}^{i\mathbf{k}_{||}\mathbf{r}_{||}}\cdot(\mathrm{e}^{ik_{z,1}z} + R_1\mathrm{e}^{-ik_{z,1}z}) \qquad z > 0 \tag{7a}$$

$$\Psi_2^1(\mathbf{r}) = \mathrm{e}^{i\mathbf{k}_{||}\mathbf{r}_{||}}\cdot(T_2\mathrm{e}^{ik_{z,2}z} + R_2\mathrm{e}^{-ik_{z,2}z}) \qquad 0 > z > -d \tag{7b}$$

$$\Psi_3^1(\mathbf{r}) = \mathrm{e}^{i\mathbf{k}_{||}\mathbf{r}_{||}}\cdot T_3\mathrm{e}^{ik_{z,3}(z+d)} \qquad -d > z \tag{7c}$$

where $k_{||}$ and k_z are the parallel and perpendicular components of the incident wave, respectively, and d is the film thickness. Pores are present in medium 2 (Scheme 2), so $\Psi_2^1(\mathbf{r})$ is an eigenstate that is perturbed by the potential V_2. Since we are interested in the scatterings in medium 2, $\Psi_2^1(\mathbf{r})$ will be written as $\Psi_{\mathrm{i}}(\mathbf{r})$. To indicate that it is an incoming wave, the wave vector $k_{z,2}$ is written as $k_{z,\mathrm{i}}$, and $k_{z,\mathrm{f}}$ denotes the wave vector of the outgoing scattered wave in medium 2. The other eigenstate, i.e., the scattered wave, can be represented by a time reversal state of the incoming wave:

$$\Psi_{\mathrm{f}}(\mathbf{r}) = \mathrm{e}^{i\mathbf{k}_{||}\mathbf{r}_{||}}\cdot({T^*}_2\mathrm{e}^{ik^*_{z,\mathrm{f}}z} + {R^*}_2\mathrm{e}^{-ik^*_{z,\mathrm{f}}z}) \tag{8}$$

To clarify whether the X-ray wave is incoming or outgoing, T_2, T^*_2, R_2, and R^*_2 are rewritten as T_i, T^*_{f}, R_i, and R^*_{f}, respectively. The superscript * indicates the complex conjugate. After inserting the eigenstates into eq 3 and carrying out rigorous algebra, one can obtain the following equation for the amplitude of the scattered wave:

$$\Psi_{\mathrm{sc}}(\mathbf{r}) = -\frac{\mathrm{e}^{ik_0r}}{4\pi r}\int {\Psi^*}_{\mathrm{f}}(\mathbf{r})\ V_2\Psi_{\mathrm{i}}(\mathbf{r})$$

$$= -\frac{\mathrm{e}^{ik_0r}}{4\pi r}\int \mathrm{d}^2{r'}_{||}\mathrm{e}^{-iq_{||}r'}[T_{\mathrm{i}}T_{\mathrm{f}}\int_{-d}^{0}\mathrm{d}z'\ \mathrm{e}^{-iq_{1,z}z'}V_2(r',z') +$$
$$T_{\mathrm{i}}R_{\mathrm{f}}\int_{-d}^{0}\mathrm{d}z'\ \mathrm{e}^{-iq_{2,z}z'}V_2(r',z') + T_{\mathrm{f}}R_{\mathrm{i}}\int_{-d}^{0}\mathrm{d}z'\ \mathrm{e}^{-iq_{3,z}z'}V_2(r',z') +$$
$$R_{\mathrm{i}}R_{\mathrm{f}}\int_{-d}^{0}\mathrm{d}z'\ \mathrm{e}^{-iq_{4,z}z'}V_2(r',z')\ ] \tag{9}$$

where $q_{1,z} = k_{z,\mathrm{f}} - k_{z,\mathrm{i}}$, $q_{2,z} = -k_{z,\mathrm{f}} - k_{z,\mathrm{i}}$, $q_{3,z} = k_{z,\mathrm{f}} + k_{z,\mathrm{i}}$, and $q_{4,z} = -k_{z,\mathrm{f}} + k_{z,\mathrm{i}}$.

Equation 9 can also be expressed in the following simpler form:

$$\Psi_{\mathrm{sc}}(\mathbf{r}) = -\frac{\mathrm{e}^{ik_0r}}{4\pi r}(T_{\mathrm{i}}T_{\mathrm{f}}F(q_{||},q_{1,z}) + T_{\mathrm{i}}R_{\mathrm{f}}F(q_{||},q_{2,z}) + T_{\mathrm{f}}R_{\mathrm{i}}F(q_{||},q_{3,z}) + R_{\mathrm{i}}R_{\mathrm{f}}F(q_{||},q_{4,z})) \quad (10)$$

where F is the amplitude of scattering from the pores in the film and $q_{||} = \sqrt{q_x{}^2 + q_y{}^2}$. Here, the size of the pores is assumed to be small compared to the film thickness d.

The intensity (I_{GISAXS}) of the wave scattered from the thin film sample (i.e., medium 2 in Scheme 2) can then be expressed as the sum of two terms as follows:

$$I_{\mathrm{GISAXS}} = \frac{\mathrm{d}\sigma}{\mathrm{d}\Omega} = r^2\{\Psi_{\mathrm{sc}}(\mathbf{r})\cdot\Psi^*_{\mathrm{sc}}(\mathbf{r})\} = \frac{1}{16\pi^2}(I_{\mathrm{independent}} + I_{\mathrm{cross}}) \quad (11)$$

where $\mathrm{d}\sigma/\mathrm{d}\Omega$ is the differential cross section of the porous film, and $I_{\mathrm{independent}}$ and I_{cross} are the independent scattering and cross terms, respectively.

In the above equations, $F(q_{||},q_{1,z})$ is not a simple Fourier transform of the scattering potential, i.e., electron density; furthermore, its complex product $|F(q_{||},q_{1,z})|^2$ contains the complex scattering vector component q_z. Thus, we have attempted to derive the $|F(q_{||},q_{1,z})|^2$ term in a manner similar to that used by Rauscher et al.[20] to derive the scattered intensity for particles in a thick substrate using a correlation function. We obtained the following expression:

$$|F(q_{||},q_{1,z})|^2 = \int \mathrm{d}^2\mathbf{r}_{||}\mathrm{e}^{-i\mathbf{q}_{||}\mathbf{r}_{||}}\int_{-d}^{0}\mathrm{d}z'\int_{-d}^{0}\mathrm{d}z''\mathrm{e}^{-iq_{1,z}z'}\mathrm{e}^{iq^*_{1,z}z'}C_w(|\mathbf{r}_{||}|,z',z'') \quad (12)$$

where $C_w(|\mathbf{r}_{||}|,z',z)$ is the correlation function. We can assume that the correlation function depends on the relative distance between pores that are homogeneously distributed in the film. Then $C_w = C_w(|\mathbf{r}_{||}|,|z|)$ with $z = z' - z''$. Splitting the (z' and z'') integration in eq 12 into two parts and interchanging the names of $z'$and z'', we obtain

$$|F(q_{||},q_{1,z})|^2 = \int \mathrm{d}^2\mathbf{r}_{||}\mathrm{e}^{-i\mathbf{q}_{||}\mathbf{r}_{||}} \times \{\int_0^d \mathrm{d}z''\int_{z'}^{d}\mathrm{d}z'\mathrm{e}^{-i\mathrm{Re}(q_{1,z})[z'-z'']}\mathrm{e}^{-\mathrm{Im}(q_{1,z})[z'+z'']}C_w(|\mathbf{r}_{||}|,|z|) + \int_0^d \mathrm{d}z''\int_{z}^{d}\mathrm{d}z''\mathrm{e}^{i\mathrm{Re}(q_{1,z})[z'+z'']}\mathrm{e}^{-\mathrm{Im}(q_{1,z})[z'+z'']}C_w(|\mathbf{r}_{||}|,|z|)\} \quad (13)$$

where $\mathrm{Im}(x)$ is the imaginary part of x. After substitution of z' by $z = |z' - z''|$, we can combine the integrals. The integral over z'' can be evaluated analytically. Unlike the case of Rauscher et al.,[20] we do not need to introduce a cutoff parameter to prevent divergence at $\mathrm{Im}(q_{1,z}) = 0$ because the film thickness is specified as d. Thus, we obtain

$$|F(q_{||},q_{1,z})|^2 = \frac{1 - \mathrm{e}^{-2\mathrm{Im}(q_{1,z})z}}{2\mathrm{Im}(q_{1,z})}\int \mathrm{d}^3\mathrm{r}\mathrm{e}^{-i\mathrm{q}_{||}\mathrm{r}_{||}}\mathrm{e}^{-i\mathrm{Re}(q_{1,z})z}\mathrm{e}^{-\mathrm{Im}(q_{1,z})|z|}C_w(\mathbf{r}) \quad (14)$$

where $\mathbf{r} = (\mathbf{r}_{||},z)$. In this equation, when $\mathrm{Im}(q_{1,z}) = 0$, the asymptotic value of the first term (i.e., $(1 - \mathrm{e}^{-2\mathrm{Im}(q1,z)d})/2\mathrm{Im}(q_{1,z})$) is d; moreover, the last term (i.e., $\mathrm{e}^{-\mathrm{Im}(q_{1,z})|z|}$) can be assigned a value of unity (= 1) for the case in which the pore size is much smaller than the scattering depth. Since an X-ray beam easily penetrates through the film when the incident angle α_{i} is greater than the critical angle of film ($\alpha_{\mathrm{c,f}}$), eq 14 can be rewritten as follows:

$$|F(q_{||},q_{1,z})|^2 = \frac{1 - \mathrm{e}^{-2\mathrm{Im}(q_{1,z})d}}{2\mathrm{Im}(q_{1,z})}I_1(q_{||},\mathrm{Re}(q_{1,z})) \quad (15)$$

where the scattering intensity of the pores, $I_1(q_{||},\mathrm{Re}(q_{1,z}))$, is the three-dimensional Fourier transform of $C_w(\mathbf{r})$, which can be calculated kinematically.

In the same manner, the other three complex product terms are calculated. However, it is noted that when the imaginary part of q_z is negative, the terms containing an imaginary q_z component (i.e., absorption terms) diverge, as observed in the case of $q_{2,z}$ and $q_{4,z}$. In fact, when scattering occurs toward the $-k_{z,\mathrm{f}}$ direction, the scattered beam is going out along the $k_{z,\mathrm{f}}$ direction and its absorption takes place during going out on to detector plane. When the incidence angle α_{i} is greater than $\alpha_{\mathrm{c,f}}$, the absorption term depends only on $k_{z,\mathrm{f}}$ wave vectors with an imaginary part, whose out-of-plane exit angle (α_{f}) is smaller than the critical exit angle of the film; the absorption term tends to be unity for $\alpha_{\mathrm{f}} < \alpha_{\mathrm{c,f}}$ and, otherwise, to be much smaller than unity for $\alpha_{\mathrm{f}} > \alpha_{\mathrm{c,f}}$. Indeed, the imaginary terms of all q_z components can be written as $\mathrm{Im}(q_z) = |\mathrm{Im}(k_{z,\mathrm{f}})| + |\mathrm{Im}(k_{z,\mathrm{i}})|$.

Taking these derivations and characteristics into account, $I_{\mathrm{independent}}$ (i.e., eq 11) can be written as follows:

$$I_{\mathrm{independent}}(\alpha_{\mathrm{f}},2\theta_{\mathrm{f}}) = \frac{1 - \mathrm{e}^{-2\mathrm{Im}(q_z)\cdot d}}{2\mathrm{Im}(q_z)}[|T_{\mathrm{i}}T_{\mathrm{f}}|^2 I_1(q_{||},\mathrm{Re}(q_{1,z})) + |T_{\mathrm{i}}R_{\mathrm{f}}|^2 I_1(q_{||},\mathrm{Re}(q_{2,z})) + |T_{\mathrm{f}}R_{\mathrm{i}}|^2 I_1(q_{||},\mathrm{Re}(q_{3,z})) + |R_{\mathrm{i}}R_{\mathrm{f}}|^2 I_1(q_{||},\mathrm{Re}(q_{4,z}))] \quad (16)$$

where α_{f} is the angle between the scattered beam and the film surface (i.e., out-of-plane exit angle), $2\theta_{\mathrm{f}}$ is the angle between the scattered beam and the plane of incidence (i.e., in-plane exit angle), and $\mathrm{Re}(x)$ is the real part of x. As shown in Scheme 2, the detector plane is defined by rectangular coordinates with two perpendicular axes, α_{f} and $2\theta_{\mathrm{f}}$.

Here it is worth considering the ensemble average of the scattered intensities from pores in the film over the pore size distribution and other parameters related to the film and the scattering measurement. The ensemble average of $I_{\mathrm{independent}}$, which is expressed by eq 11, can be performed in a straightforward manner because $I_{\mathrm{independent}}$ is always positive; the ensemble average of the scattered intensities of particles is well described in the literature.[21,24] In contrast to $I_{\mathrm{independent}}$, the ensemble average of I_{cross} should be performed with care because I_{cross} may be positive or negative depending on several factors. First, the parameter R_{i} in the expression for I_{cross} may be positive or negative depending on the incident angle of the X-ray beam, the refractive index and thickness of the film, the pore size distribution, and the divergence of the incident X-ray beam. Second, the products of F terms and their complex terms in the expression for I_{cross} are not always in the same phase. The frequency of the phase (i.e., positive or negative) variation becomes faster as the film thickness increases. These products also vary depending on the pore size distribution and are additionally sensitive to any incoherence in the incident X-ray beam. Because of the contributions of these factors, the ensemble average of I_{cross} either vanishes completely or is sufficiently small that it can be neglected. Therefore, for these cases, I_{GISAXS} (i.e., eq 11) can be approximated by the following expression:

$$I_{\mathrm{GISAXS}}(\alpha_{\mathrm{f}},2\theta_{\mathrm{f}}) \cong \frac{1}{16\pi^2}\frac{1 - \mathrm{e}^{-2\mathrm{Im}(q_z)\cdot d}}{2\mathrm{Im}(q_z)}[|T_{\mathrm{i}}T_{\mathrm{f}}|^2 I_1(q_{||},\mathrm{Re}(q_{1,z})) + |T_{\mathrm{i}}R_{\mathrm{f}}|^2 I_1(q_{||},\mathrm{Re}(q_{2,z})) + |T_{\mathrm{f}}R_{\mathrm{i}}|^2 I_1(q_{||},\mathrm{Re}(q_{3,z})) + |R_{\mathrm{i}}R_{\mathrm{f}}|^2 I_1(q_{||},\mathrm{Re}(q_{4,z}))] \quad (17)$$

However, in the case of a film containing monodisperse pores and a coherent X-ray beam, the ensemble average of I_{cross} cannot be neglected. Taking into account the approximation that the imaginary terms of all q_z components can be written as $\mathrm{Im}(q_z)$, as discussed in the derivation of $I_{\mathrm{independent}}$ in eq 16, F in eq 10 can be treated as a simple Fourier transform of the scattering potential. Therefore, I_{GISAXS} (i.e., eq 11) can be rewritten by the following simplified expression:

$$I_{\mathrm{GISAXS}}(\alpha_f,2\theta_f) = \frac{1}{16\pi^2}\frac{1-\mathrm{e}^{-2\mathrm{Im}(q_z)\cdot d}}{2\mathrm{Im}(q_z)}|T_iT_fF(q_{||},\mathrm{Re}(q_{1,z})) + T_iR_fF(q_{||},\mathrm{Re}(q_{2,z})) + T_fR_iF(q_{||},\mathrm{Re}(q_{3,z})) + R_iR_fF(q_{||},\mathrm{Re}(q_{4,z}))|^2 \quad (18)$$

Equations 17 and 18 indicate that scattering from pores buried in the film coated onto a substrate takes place through four main types of processes: (i) the incident beam scatters without reflection, (ii) the scattered beam is reflected at the interface between the film and the substrate, (iii) the reflected beam scatters, and (iv) the scattered, reflected beam is reflected once more.

For a given porous film, the overall GISAXS pattern generated by eq 18 was found to be nearly the same as that generated by eq 17. However, the GISAXS pattern generated by eq 18 more clearly shows the oscillation frequency arising from the thickness of the film. On the other hand, when the analytical formula for the scattering amplitudes is not easily obtained, eq 17 is very useful for calculating scattering intensities from pores in thin films even though the cross terms give rise to some minor errors in the intensity near the critical angle. Therefore, one can use either eq 17 or eq 18, depending on the circumstances.

Results and Discussion

TGA Analysis. The PMSSQ precursor was heated at a rate of 2.0 °C/min, under a nitrogen atmosphere, and subsequently cured between 75 and 340 °C (Figure 1). This reaction was accompanied by weight losses due to the losses of water and ethanol byproducts. The cured PMSSQ product finally underwent thermal decomposition above 500 °C. The star-shaped PCL4 porogen decomposed above 205 °C, where decomposition was complete above 352 °C, leaving no residue. When the PCL4 porogen is embedded within the PMSSQ precursor matrix, however, the porogen undergoes thermal decomposition at 293 °C, regardless of the loading over the range 10−40 wt % (see Figure 1). This high decomposition temperature is thought to be due to the probable hybridization of the porogen hydroxyl end groups with the ethoxy and hydroxyl groups of the PMSSQ precursor, possibly prior to porogen decomposition.

TEM Analysis. A representative TEM image of the porous PMSSQ film is shown in Figure 2. The image clearly shows that the nanopores generated in the dielectric film by the sacrificial thermal degradation of the PCL4 porogen are spherical in shape and that their sizes are around 5 nm.

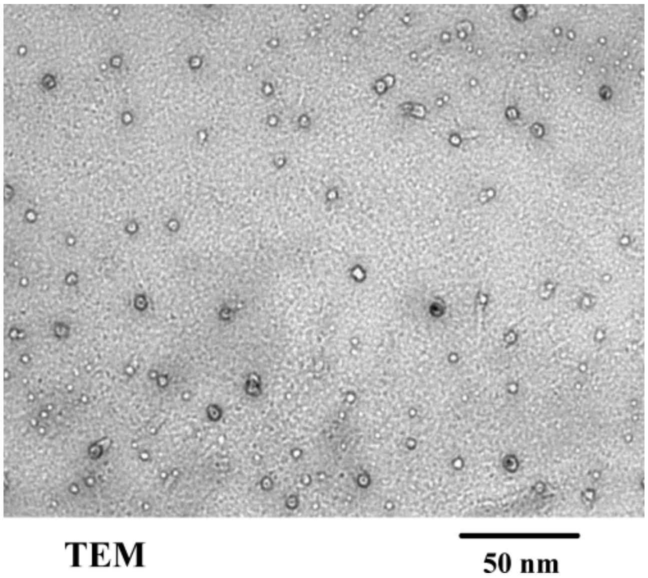

Figure 2. TEM image of a nanoporous PMSSQ dielectric prepared from a PMSSQ precursor sample loaded with 10.0 wt % PCL4.

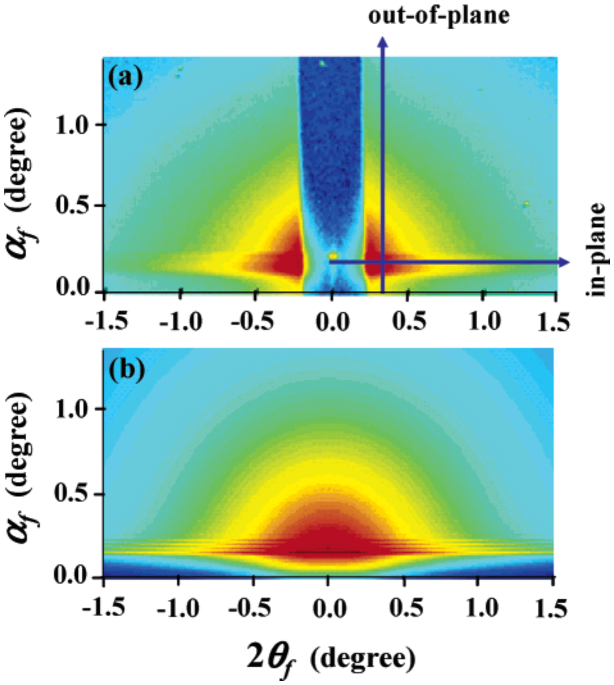

Figure 3. (a) 2D GISAXS pattern measured at $\alpha_i = 0.20°$ for a 108 nm thick porous film derived from a PMSSQ precursor film loaded with 20 wt % PCL4. (b) GISAXS pattern calculated for the porous film in (a) using the GISAXS formula (eq 17); in this calculation, pores are spherical in a log−normal size distribution ($r_0 = 3.73$ and $\sigma = 0.523$) (see eqs 19 and 20); the electron densities of the porous film and silicon substrate are 324 and 699.5 nm^{-3}, respectively, and the film thickness is 108 nm.

Static GISAXS Analysis. Taking the TGA results into account, GISAXS measurements were carried out on porous PMSSQ dielectric films imprinted with various PCL4 porogen loadings; here the porous films were prepared by thermal treatment up to 400 °C. Figure 3a shows a typical 2D GISAXS pattern of a nanoporous PMSSQ film imprinted with a 20 wt % PCL4 loading. Similar GISAXS patterns were obtained for nanoporous PMSSQ films prepared with different porogen loadings (data not shown). As can be seen in Figure 3a, brightly striped patterns appear along $2\theta_f$ (i.e., q_y direction) at the exit angles (α_f) between the critical angles of the film and the silicon substrate ($\alpha_{c,f}$ and $\alpha_{c,s}$). These striped patterns are intense scatterings formed due to the combination of a type of standing wave phenomenon and total reflection at the interface between the film and the substrate (i.e., the T_f and R_f terms in eq 17 or eq 18), as often observed on specular X-ray reflectivity patterns.[18] When the electric fields of the incoming and out-going reflected X-ray beams are in phase at a certain incident angle, the electric fields of the X-ray waves constructively interfere and are waveguided through the film, consequently enhancing the intensity of the scattered waves from the pores inside of film. From such enhanced GISAXS patterns, however, it is very difficult to determine the positions of the pores along the z-direction (i.e., thickness direction) of the porous film because the pores are randomly distributed in the film (see the TEM image in Figure 2).

As described above, the striped patterns observed between $\alpha_{c,f}$ and $\alpha_{c,s}$ are bright, but their fringes (which are the oscillations mainly due to the film thickness) are not clearly shown. The TEM image of Figure 2 indicates that the generated pores have a certain degree of size variation. Moreover, the GISAXS measurements of our study were carried out using an incoherent rather than a coherent X-ray beam. Taking these facts into account, the I_{cross} term in eq 11 (or eq 18) can be neglected. Therefore, we attempted to analyze all of the GISAXS data in our study by using eq 17.

Considering the observed GISAXS characteristics, in-plane GISAXS profiles were extracted at $\alpha_f = 0.17°$ (i.e., an exit angle between the $\alpha_{c,f}$ and $\alpha_{c,s}$) from the measured 2D GISAXS patterns, while out-of-plane GISAXS profiles were taken at $2\theta_f = 0.25°$. The extracted scattering profiles are shown in Figures 4a and 5.

To analyze these scattering profiles by using the GISAXS formula (eq 17), we examined all possible scattering models for the scattered intensity from pores in the dielectric film (i.e., I_1 term in eq 17). We found that the following equation for I_1 derived under kinematic theory is the most suitable for analyzing the measured GISAXS profiles with the GISAXS formula:

$$I_1 = c\int_0^{\infty} n(r_p)\, v^2(r_p)\, |F_S(qr_p)|^2\, S_S(qr_p)\, \mathrm{d}r_p \qquad (19)$$

where c is a constant, $v(r_p)$ is the volume of each pore, $F_S(qr_p)$ is the spherical form factor, and $S_S(qr_p)$ is the structure factor for the monodisperse hard-sphere model.[24] $n(r_p)$ is the log−normal pore size distribution function:

$$n(r_p) = \frac{1}{\sqrt{2\pi} r_0 \sigma \mathrm{e}^{\sigma^2/2}} \mathrm{e}^{-\ln(r_p/r_o)^2/2\sigma^2} \qquad (20)$$

where r_p is the pore radius, and r_0 and σ are the pore radius corresponding to the peak maximum and the width in the radius distribution, respectively.

As seen in Figure 4a, the extracted in-plane GISAXS scattering profiles of the porous films, imprinted with 10−20 wt % PCL4 porogen loadings, show a good fit with the GISAXS formula, suggesting that the pores are spherical in shape. However, the scattering profiles of the porous films prepared with higher porogen loadings could not be fitted to the GISAXS formula since the pore sizes are too large and thus outside the detection limit (ca. 40 nm) for the current GISAXS setup. These GISAXS analyses determined pore size and size distribution. As can be seen in Figure 4b and Table 1, films imprinted with only a 10 wt % porogen loading have pores with $\overline{r_p}$ (average radius of the most populated pores in the size distribution) of 3.3 nm, $\overline{R_g}$ (average radius of gyration) of 8.8 nm, and a relatively narrow size distribution ($\sigma = 0.444$). As the PCL4 loading was increased to 20 wt %, pores of much larger size ($\overline{r_p}$ = 5.6 nm and $\overline{R_g}$ = 15.8 nm), and broader distribution (σ = 0.523) were generated in the PMSSQ films. Further increases in the PCL4 porogen loading (up to 30−40 wt %) were found to create large pores in the dielectric films. These results indicate that the PCL4 porogen molecules have a tendency to segregate in the PMSSQ matrix, a tendency that is enhanced as the porogen loading is increased.

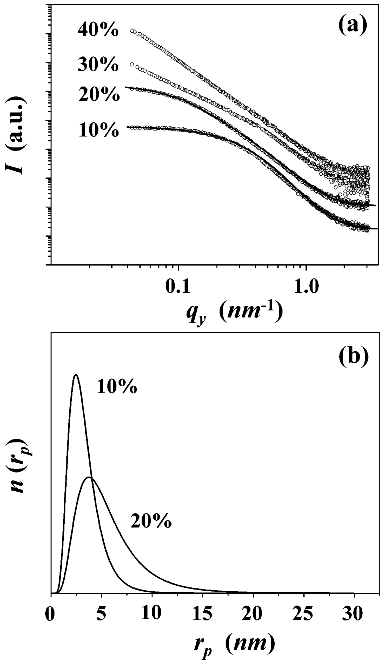

Figure 4. (a) In-plane GISAXS profiles extracted along the q_y direction at $\alpha_f = 0.17°$ from the 2D GISAXS patterns measured for nanoporous PMSSQ films: the symbols represent the measured data, and the solid lines were obtained by fitting the data with the GISAXS formula eq 17. (b) Pore radius and distribution determined from the GISAXS analysis of the in-plane scattering profile data in (a). The notation used indicates the initial porogen loading in wt %.

Table 1. Pore Structures and Properties of Nanoporous PMSSQ Dielectric Films Imprinted with PCL4 Porogen[a]

	pore size and size distribution				properties		
porogen loading (wt %)	r_0[b] (nm)	σ[d]	$\overline{r_p}$[f] (nm)	$\overline{R_g}$[g] (nm)	$\alpha_{c,f}$[h] (deg)	ρ_e[i] (nm^{-3})	P[j] (%)
0					0.185	396	0
10	2.45 (0.02)[c]	0.444 (0.004)[e]	3.27	8.77	0.174	356	10.2
20	3.73 (0.04)	0.523 (0.006)	5.62	15.79	0.166	324	18.2
30	—[k]	—[k]	—[k]	—[k]	0.153	275	30.5
40	—[k]	—[k]	—[k]	—[k]	0.141	234	41.0

[a] Porous dielectric films were prepared by thermal treatments of their PMSSQ precursor/PCL4 porogen composite films at 400 °C in a vacuum. [b] Pore radius determined from the peak maximum of the radius r_p and the number distribution of pores. [c] Standard deviation in the pore radius. [d] Width of the radius r_p and the number distribution of pores. [e] Standard deviation in the width of the distribution. [f] Average pore radius determined from the radius r_p and the number distribution of pores. [g] Average radius of gyration estimated from the radius r_p and the number distribution of pores. [h] Critical angle of film determined from the out-of-plane GISAXS profile. [i] Electron density determined from the critical angle of film. [j] Porosity estimated from the electron density of the film. [k] Not detected due to the out of the detection limit (ca. 40 nm).

Figure 5 shows the out-of-plane GISAXS profiles for nanoporous PMSSQ films. The out-of-plane GISAXS scattering profiles of the porous films, imprinted with 10−20 wt % PCL4 porogen loadings, show a good fit to the GISAXS formula along with the pore parameters obtained from the analysis of the in-plane GISAXS profiles, confirmed that the pore size and pore size distribution are isotropic in the dielectric films. These results indicate that the procedure used—spin-coating,

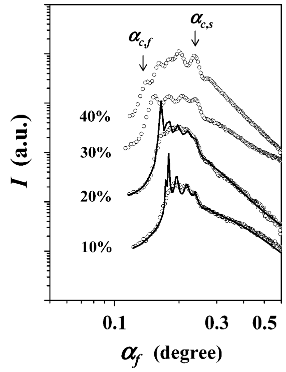

Figure 5. Out-of-plane GISAXS profiles extracted at $2\theta_f = 0.25°$ from the 2D GISAXS patterns of nanoporous PMSSQ films imprinted with the PCL4 porogen: the symbols represent the measured data, and the solid lines were obtained by fitting the data with the GISAXS formula, eq 17. The notation used indicates the initial porogen loading in wt %. The thicknesses of the porous films imprinted with 10 and 20 wt % PLC4 were 90 and 108 nm, respectively.

drying, and thermal processing—does not induce any anisotropy in the pore shape and size in the nanoporous films.

As seen in Figure 5, each scattering profile shows oscillations between the $\alpha_{c,f}$ and $\alpha_{c,s}$, formed due to the combination of a type of standing wave phenomenon and total reflection at the interface between the film and the substrate, as mentioned above. The $\alpha_{c,f}$ clearly decreases with increasing initial porogen loading, whereas the $\alpha_{c,s}$ is insensitive to porogen loading. From the $\alpha_{c,f}$ values, the electron densities (ρ_e) of the films were determined using the following relation:[7]

$$\rho_e = \frac{\pi \alpha_{c,f}^{\ 2}}{r_e \lambda^2} \tag{21}$$

where r_e is the classical radius (2.818×10^{-15} m) of the electron and λ is the wavelength of the X-ray beam used in the GISAXS measurement. The film porosities were further estimated from the electron densities of the films, with respect to that of the PMSSQ film prepared in the absence of porogen. The results are summarized in Table 1. The porosities of the nanoporous films were found in the range 10.2−41.0%, depending on the initial porogen loadings.

From the parameters obtained above, we have attempted to calculate 2D GISAXS patterns using the GISAXS formula. One of the obtained patterns is shown in Figure 3b, which was calculated for the porous film imprinted with 20 wt % PCL4. This pattern compares well with the measured pattern (Figure 3). For the porous film imprinted with 10 wt % PCL4, the calculated pattern was also found to compare well with the measured pattern (data not shown).

In-Situ GISAXS Analysis. In-situ GISAXS measurements were carried out in order to establish the mechanism for pore generation in the PMSSQ precursor and PCL4 porogen composite films. These measurements were performed on the composite films during both heating (up to 400 °C) and subsequent cooling of the resulting porous films. For 2D GISAXS, patterns obtained for each composite film, both in-plane and out-of-plane GISAXS profiles were extracted at $\alpha_f = 0.17°$ and $2\theta_f = 0.25°$, respectively.

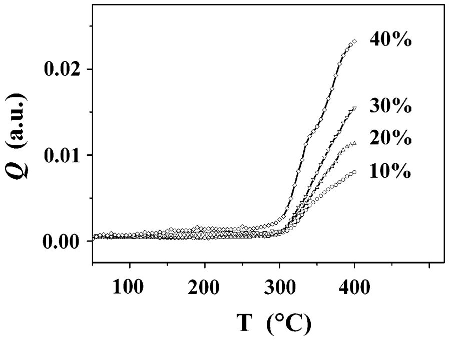

Figure 6. Temperature dependence of the invariant *Q* values obtained from in-plane GISAXS (which was extracted at $\alpha_f = 0.17°$) of 2D GISAXS patterns measured during heating runs with 2.0 °C/min of composite films of PMSSQ precursor and PCL4 porogen in various compositions under vacuum. The notation used indicates the initial porogen loading in wt %.

As discussed above, we found that the pore size and pore size distribution are isotropic in the dielectric films prepared in our study. Taking this finding into account, we have first attempted to determine the change in the invariant *Q* from the extracted in-plane GISAXS profiles as a function of temperature by the following equation (see ref 25 for the general definition of invariant *Q*):

$$Q = \int_{q_{y,\min}}^{q_{y,\max}} q_y^{\ 2} I_{\mathrm{GISAXS}}((\text{constant } q_z), q_y)\, \mathrm{d}q_y \tag{22}$$

Taking into consideration the known relationship between the invariant *Q* and morphological parameters in two-phase polymer systems,[25,26] the invariant *Q* in eq 25 can be expressed in terms of the volume fractions and electron densities of the components in both the composite film and the resulting porous film:

$$Q \propto \varphi_{\mathrm{PMSSQ\ precursor}} \varphi_{\mathrm{PCL4}} (\rho_{\mathrm{e(PMSSQ\ precursor)}} - \rho_{\mathrm{e(PCL4)}})^2 \tag{23a}$$

and

$$Q \propto \varphi_{\mathrm{PMSSQ}} \varphi_{\mathrm{pore}} (\rho_{\mathrm{e(PMSSQ)}} - \rho_{\mathrm{e(pore)}})^2 \tag{23b}$$

where φ_i and $\rho_{e(i)}$ represent the volume fraction and electron density of the component *i*, respectively. As seen in Table 1, the electron density ρ_e of the PMSSQ dielectric film cured at 400 °C is taken to be 396 nm^{-3} and is assumed to be zero for pores generated in the dielectric film. Taking this into account, the *Q* value in eqs 25 and 26 is therefore taken to be a maximum when all porogen molecules in a given composite film are exhausted.

A selection of *Q* values obtained for composite films with various PCL4 porogen loadings is presented in Figure 6. For a 10 wt % PCL4 loading, the value of *Q* is small at room temperature but increases very slowly with elevating temperature. The *Q* value then increases rapidly around 293 °C and continues to rise up to 400 °C. Similar *Q* variations were observed for the other composite films studied. These results provide important information regarding composite films in which the PMSSQ precursor undergoes curing, and the porogen undergoes sacrificial thermal degradation, as described below.

First, the spectroscopic ellipsometry measurements found that the refractive index n_R at 633 nm is 1.4265 for the PMSSQ precursor and 1.4863 for the PCL4 porogen. In addition, X-ray reflectivity measurements showed that the porogen ρ_e value is slightly larger than that of the precursor.[18] Moreover, it is important to note that all of the composite films studied here are optically clear. The low Q values obtained at room temperature are attributed to the small difference between the ρ_e values of the precursor and porogen components, as well as to the small degree of phase separation if phase separation is involved in the spin-coating of the homogeneous solutions and in the subsequent drying at 50 °C.

Second, as mentioned in the discussion of the TGA results (Figure 1), the PMSSQ precursor component undergoes partial thermal curing in the range 25−293 °C, while the porogen remains provided no thermal degradation takes place. The partial curing of the PMSSQ precursor was found to cause variations in both the n_R and ρ_e value. The n_R value at 633 nm was found to be 1.4265 for the PMSSQ precursor film obtained prior to curing, and 1.4058 and 1.3991, after curing at 200 and 250 °C, respectively. In addition, the 200 °C cured PMSSQ precursor film gave $\rho_e = 401$ nm^{-3}, which is slightly larger than that (396 nm^{-3}) obtained for the fully cured PMSSQ film.[18] Taking these data into account, the very slow Q value increases with temperature, in the range 25−293 °C, are caused by slight increases in the difference between the ρ_e values of the dielectric matrix and porogen components and further by phase separation if phase separation occurs.

Finally, the TGA measurements infer that the porogen molecules in the PMSSQ precursor matrix undergo sacrificial thermal degradation above 293 °C (Figure 1). Such thermal degradation produces pores with a ρ_e value much less than those of the precursor dielectric matrix and porogen; the ρ_e value of the pores is expected to be zero. Consequently, imprinting pores in the dielectric matrix film leads to a large difference between the ρ_e values of the pores and dielectric matrix and thus a large increase in the Q value. In essence, a higher population of pores in the dielectric film results in larger Q values (eq 23). Taking these into account, the rapid Q value increases above 293 °C are mainly attributed to the generation of pores with low ρ_e values in the dielectric matrix. It is important to note that the Q value is also dependent on the size and size variation of the generated pores, since the scattering intensity is a function of pore size.

Taking these Q results into account, the extracted in-plane and out-of-plane GISAXS profiles were analyzed in detail. Figure 7a,b shows representative in-plane GISAXS profiles measured during heating of the PMSSQ precursor composite film loaded with 10 wt % PCL4 porogen. The analysis results of these scattering profiles are summarized in Figure 7c as well as Table 2 and Figure 8.

As seen in Figure 7b, the in-plane GISAXS profile measured at 50 °C appears very weak and featureless. Indeed, similar featureless scattering profiles were also observed up to around 145 °C. These weak, featureless scattering profiles are first attributed to a relatively low contrast in the electron densities of the PMSSQ precursor and PCL4 porogen as mentioned above. Moreover, it is possible that the formation of very small porogen aggregates, caused by phase separation during spin-coating, and the subsequent drying process, is also a likely cause for the formation of the featureless scattering profiles. An in-plane GISAXS profile of a PMSSQ precursor film loaded with 10 wt % PCL4 porogen was calculated in order to obtain information regarding the size of such formed porogen aggregates based on the assumption that single molecules of the PCL4 porogen are well distributed within the PMSSQ precursor matrix. The $\overline{R_g}$ value for a single PCL4 porogen molecule at a Θ condition is approximated to be 1.90 nm from its molecular weight as a known relationship in the literature.[27] From this $\overline{R_g}$ value, we can further approximate the peak maximum r_0 and the width σ of the radius distribution of single porogen molecules (Table 2 and Figure 8). The calculated scattering profile obtained using the approximated r_0 and σ values is comparable with the profile measured at 50 °C (Figure 7b), particularly over the q range 0.1−1.0 nm^{-1}. These results suggest that the PCL4 porogen molecules are molecularly dispersed throughout the composite film prepared via spin-coating of its homogeneous solution in MIBK, followed by subsequent drying at 50 °C.

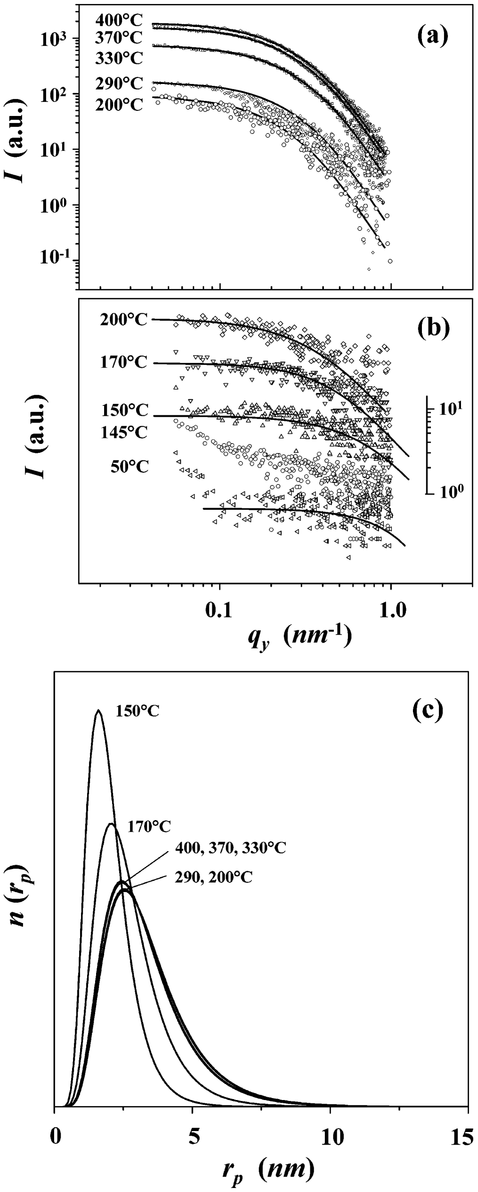

Figure 7. (a, b) In-plane GISAXS profiles at $\alpha_f = 0.17°$ of 2D GISAXS patterns measured during heating (2.0 °C/min) of a PMSSQ precursor film loaded with 10 wt % PCL4 under vacuum. (c) Pore radius and distribution determined from the GISAXS analysis of the in-plane scattering profile data in (a) and (b).

Table 2. Results of Analysis of In-Plane GISAXS Profiles Measured in-Situ during Heating Runs of PMSSQ Precursor/PCL4 Porogen Composite Films up to 400 °C and Subsequent Cooling Runs of the Resulting Porous Films[a]

	porogen loading							
	10 wt % pore size and size distribution				20 wt % pore size and size distribution			
temp (°C)	r_0[b] (nm)	σ[c]	$\overline{r_p}$[d] (nm)	$\overline{R_g}$[e] (nm)	r_0 (nm)	σ	$\overline{r_p}$ (nm)	$\overline{R_g}$ (nm)
on heating								
50	(1.00)[f]	(0.35)[f]	(1.20)[f]	(1.90)[f]	(1.00)	(0.35)	(1.20)	(1.90)
100	(1.00)	(0.35)	(1.20)	(1.90)	(1.00)	(0.35)	(1.20)	(1.90)
135	(1.00)	(0.35)	(1.20)	(1.90)	(>1.00)	(>0.35)	(>1.20)	(>1.90)
145	(1.00)	(0.35)	(1.20)	(1.90)	3.47	0.50	5.40	14.51
150	1.60	0.39	2.01	4.18	3.70	0.50	5.37	14.90
170	2.06	0.42	2.68	6.48	3.75	0.49	5.43	14.96
200	2.53	0.46	3.47	9.57	3.78	0.52	5.69	15.87
290	2.55	0.44	3.41	9.08	3.76	0.52	5.67	15.84
330	2.45	0.44	3.27	8.76	3.76	0.52	5.67	15.84
370	2.46	0.44	3.28	8.79	3.72	0.52	5.61	15.78
400	2.44	0.44	3.26	8.73	3.72	0.52	5.61	15.78
on cooling								
25	2.45	0.44	3.27	8.77	3.73	0.52	5.62	15.79

[a] GISAXS measurements were carried out at a heating and cooling rate of 2.0 °C/min in a vacuum; the samples were kept for 30 min when they reached to 400 °C and then cooled to room temperature. [b] Pore radius determined from the peak maximum of the radius r_p and the number distribution of pores. [c] Width of the radius r_p and the number distribution of pores. [d] Average pore radius determined from the radius r_p and the number distribution of pores. [e] Average radius of gyration estimated from the radius r_p and the number distribution of pores. [f] $\overline{R_g}$ of a single PCL4 porogen molecule was estimated from the molecular weight of PCL4 porogen; from the $\overline{R_g}$ value, r_0, σ, and $\overline{r_p}$ were further estimated.

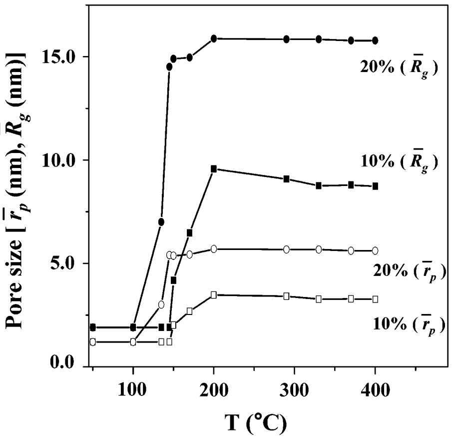

Figure 8. Pore size variations determined from the GISAXS analysis of the in-plane scattering profiles at $\alpha_f = 0.17°$ of 2D GISAXS patterns measured during heating (2.0 °C/min) of PMSSQ precursor films loaded with 10 and 20 wt % PCL4 under vacuum. The notation used indicates the initial porogen loading in wt %. $\overline{r_p}$ is the average pore radius determined from the radius r_p and the number distribution of pores; $\overline{R_g}$ is the average radius of gyration estimated from the radius r_p and the number distribution of pores.

Above 150 °C, the scattering profile begins to show structural features. Thereafter, the intensity of the scattering profile increases slightly, and its shape changes with increasing temperature up to 200 °C. The scattering profile retains its shape up to 290 °C, a temperature that is close to the onset of PCL4 porogen thermal degradation (293 °C), where only the intensity level over the measured q_y range showed a slight increase. A careful analysis of the scattering profiles, presented in Figure 7b as well as Table 2 and Figure 8, indicates that heating the PCL4 porogen component in the composite film initiates aggregation around 150 °C, which then continues up to 200 °C. With further increasing temperature, the porogen aggregates maintain their size and size distribution until they undergo thermal degradation.

Phase separation of the porogen component in the composite film is understood by considering the thermal characteristics of both the PMSSQ precursor and porogen components. An oscillating differential scanning calorimetry (oscillating DSC) study recently revealed that PMSSQ precursor films have a glass transition temperature T_g around 88−111 °C, depending on the ratio of hydroxyl and ethoxy groups within the precursor; larger values of this ratio led to higher T_g values due to the higher degree of hydrogen bonding.[28] A similar T_g is expected for the PMSSQ precursor in the composite film studied here. The melting (57 °C T_m) and glass transition (−60 °C T_g) temperature of the PCL4 porogen component were obtained via DSC measurements.[16] The PMSSQ precursor matrix, on the other hand, was found to undergo curing in a slow manner over the broad temperature range 75−340 °C, forming cross-links (Figure 1). The PMSSQ precursor, with its molecular mobility in a certain degree, undergoes curing above its T_g, while the PCL4 porogen appears highly mobilized. In general, polymers that experience a higher degree of cross-linking show increases in T_g and restricted molecular mobility. This is reflected in the heating of the PMSSQ precursor matrix during its curing phase, where the mobility becomes restricted as the degree of cross-linking increases. Taking these facts into account, phase separation of the PCL4 porogen component is first induced following curing reaction of the PMSSQ precursor component, bought on by heating. Such induced phase separations for both components continue with increasing temperature. In particular, phase separation of the PCL4 porogen component occurs readily up to 200 °C but becomes restricted immediately above this temperature due to immobilization of the PMSSQ precursor matrix. This immobilization is caused by the formation of cross-links up to 200 °C and by the resultant high T_g, which is much greater than 200 °C.

In addition, the slight increase in intensity in the scattering profile, with no accompanying change in shape over the temperature range of 200−290 °C, is clearly understood when considering the variation in electron density ρ_e of the precursor matrix during the curing phase. As discussed above, the ρ_e value of the PMSSQ precursor is slightly larger than that of the fully cured PMSSQ. However, the ρ_e value of the phase-separated PCL4 porogen aggregates, confined in the immobilized precursor matrix, varies little over the temperature range, where only very small density fluctuations occur due to heating. Thus, such slight intensity increases in the scattering profile are attributed to minor increases in the difference between the ρ_e values of the porogen and matrix components within the composite film.

Moreover, above 290 °C, the intensity of the scattering profile was found to increase with increasing temperature (up to 400 °C) while retaining its shape (Figure 7a). These intensity increases with temperature are attributed to pores created in the film by the thermal degradation of the porogen aggregates above 293 °C. From an analysis of the scattering profiles, the size and size distribution of pores imprinted in the film were found to be almost identical to those of the porogen aggregates developed below 200 °C (Table 2). These results indicate that above 293 °C the individually occupied porogen aggregates confined within the immobilized PMSSQ precursor matrix undergo sacrificial thermal degradation without further aggregation. This ultimately results in the imprinting of pores within the cured matrix film, with sizes equivalent to those of the porogen aggregates.

A similar trend was observed in the in-plane GISAXS profiles obtained during heat treatment of the PMSSQ precursor composite films containing a 20 wt % PCL4 porogen loading (data not shown). The analysis results of the measured scattering profiles are summarized in Table 2 and Figure 8. In the case of this composite film, only two differences were observed compared to the results obtained for the composite film loaded with 10 wt % porogen. First, the phase separation of the porogen, caused by curing of the PMSSQ precursor matrix, was found to start at 135 °C, which is lower than that (150 °C) of the 10 wt % porogen loaded composite film. Second, the porogen aggregates developed in the composite film were found to have relatively larger sizes and broader size distributions than those of the 10 wt % porogen loaded composite film. These results indicate that at higher loadings the PCL4 porogen in the PMSSQ precursor film undergoes phase separation during heating at lower temperature, resulting in the formation of relatively larger-sized porogen aggregates with broader size distributions. The size and distribution of these same aggregates were also reflected in the imprinted pores.

Figure 9 shows representative out-of-plane GISAXS profiles, which were extracted from the 2D GISAXS patterns measured during the heating of a PMSSQ precursor composite film with a 30 wt % PCL4 porogen loading. Here, a variation in the critical angle of the composite film $\alpha_{c,f}$ with increasing temperature is clearly evident (Figure 9). The $\alpha_{c,f}$ value of 0.186° at 50 °C shows a very slow shift toward the low angle region as the temperature draws closer to 293 °C. This is due to the removal of the water and ethyl alcohol byproducts, formed in the composite film during the curing of the precursor matrix component. Above 293 °C, the $\alpha_{c,f}$ shows a dramatic shift toward the low angle region as the temperature is increased, achieving a final value of 0.153° at 400 °C. This drastic shift in $\alpha_{c,f}$ toward the low angle region is attributed primarily to the electron density of the film, which is lowered when pores are imprinted in the film through the thermal degradation of the porogen aggregates and partly lowered following removal of the water and ethyl alcohol byproducts from the composite film. Similar trends in the $\alpha_{c,f}$ variation with temperature were observed in the out-of-plane GISAXS profiles of other composite films studied (data not shown).

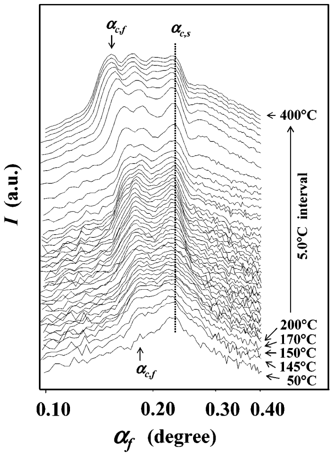

Figure 9. Out-of-plane GISAXS profiles at $2\theta_f = 0.25°$ of 2D GISAXS patterns measured during heating (2.0 °C/min) of a PMSSQ precursor film loaded with 30 wt % PCL4 under vacuum. $\alpha_{c,f}$ and $\alpha_{c,s}$ indicate the critical angles of the composite film and silicon substrate, respectively.

The combined results suggest that thermal curing of the PMSSQ precursor component leads to phase separation of the PCL4 porogen, generating porogen aggregates of a certain size and size distribution. Moreover, the sacrificial thermal degradation of these porogen aggregates produces imprinted pores in the composite film with the same size and size distribution as the initial porogen aggregates. Higher porogen loading in the precursor film results in larger-sized porogen aggregates with broader size distributions, due to the induced phase separation bought on by curing of the precursor, ultimately realizing larger-sized nanopores with broader size distributions.

Conclusions

In-situ GISAXS measurements were successfully performed on nanopores imprinted within PMSSQ precursor films, formed by the thermal degradation of a four-armed PCL4 porogen on heating to 400 °C. A GISAXS theory, based on the distorted wave Born approximation (DWBA), showed good comparison with the measured GISAXS patterns. Both the in-situ GISAXS measurements and the data analysis obtained using the GISAXS theory provided important structural information (i.e., size, size distribution, shape, and electron density) for the thermally treated composite thin films of the PMSSQ precursor and PCL4 porogen and for the resulting nanoporous films.

In addition, the in-situ GISAXS analyses helped establish a mechanism for the formation of imprinted nanopores within the PMSSQ film. Here, heating of the porogen-loaded PMSSQ precursor matrix caused a curing reaction of the precursor matrix component, leading the phase separation of the porogen component. The sacrificial thermal degradation of the developed porogen aggregates afforded imprinted nanopores within in the film. Such phase separation occurred mainly below 200

°C. Above this temperature, no further phase separation occurred due to the high degree of cross-links formed through curing, effectively immobilizing the matrix. The phase separation of porogen was further dependent on the porogen loading level in the composite film; higher porogen loadings resulted in larger porogen aggregates and greater size distributions. The developed porogen aggregates remained confined within the matrix film without any further growth or movement until the temperature reached 293 °C (i.e., onset of porogen thermal degradation). Here, the porogens were effectively removed from their individual locations through heating, leaving their individual footprints in the film as spherical nanopores. The nanopore size and size distribution were identical to those of the porogen aggregates prior to thermal degradation. Conclusively, the pore size, size distribution, shape, and pore distribution within the PMSSQ film are all governed by the porogen aggregates produced as a result of phase separation, induced by curing of the PMSSQ precursor occurred over the broad temperature range 75−340 °C.

In summary, this study provides the first demonstration that in-situ GISAXS is a powerful tool for monitoring the evolution of nanopores in nanoporous dielectric thin films, providing structural characteristics (i.e., size, size distribution, shape, electron density, and porosity) as a function of thin film process parameters such as temperature and time.

Acknowledgment. This study was supported by the Center for integrated Molecular Systems (KOSEF). Synchrotron GISAXS measurements were supported by MOST and POSCO.

Note Added after ASAP Publication. This article was released ASAP on March 8, 2005. Equations 8, 18, and 19 and the text following eq 9 have been revised. The revised version was posted on March 15, 2005.

References and Notes

(1) (a) Miller, R. D. *Science* **1999**, *286*, 421. (b) Maex, K.; Baklanov, M. R.; Shamiryan, D.; Iacopi, F.; Brongersma, S. H.; Yanovitskaya, Z. S. *J. Appl. Phys.* **2003**, *93*, 8793. (b) Morgen, M.; Ryan, E. T.; Zhao, J.-H.; Hu, C.; Cho, T.; Ho, P. S. *Annu. Rev. Mater. Sci.* **2000**, *30*, 645. (c) Maier, G. *Prog. Polym. Sci.* **2001**, *26*, 3. (d) Ree, M.; Goh, W. H.; Kim, Y. *Polym. Bull.* **1995**, *35*, 215.

(2) Dultsev, F. N.; Baklanov, M. R. *Electrochem. Solid-State Lett.* **1999**, *2*, 192.

(3) Huang, E.; Toney, M. F.; Volksen, W.; Mecerreyes, D.; Brock, P.; Kim, H.-C.; Hawker, C. J.; Hedrick, J. L.; Lee, V. Y.; Magbitang, T.; Miller, R. D. *Appl. Phys. Lett.* **2002**, *81*, 2232.

(4) (a) Lee, H.-J.; Lin, E. K.; Wang, H.; Wu, W.-L.; Chen, W.; Moyer, E. C. *Chem. Mater.* **2002**, *14*, 1845. (b) Yang, S.; Mirau, P. A.; Pai, C.-S.; Nalamasu, O.; Reichmanis, E.; Lin, E. K.; Lee, H.-J.; Gidley, D. W.; Sun, J. *Chem. Mater.* **2001**, *13*, 2762.

(5) Kim, H.-C.; Volksen, W.; Miller, R. D.; Huang, E.; Yang, G.; Briber, R. M.; Shin, K.; Satija, S. K. *Chem. Mater.* **2003**, *15*, 609.

(6) Yang, G. Y.; Briber, R. M.; Huang, E.; Rice, P. M.; Volksen, W.; Miller, R. D. *ACS Polym. Mater. Sci. Eng.* **2001**, *85*, 18.

(7) (a) Bolze, J.; Ree, M.; Youn, H. S.; Chu, S.-H.; Char, K. *Langmuir* **2001**, *17*, 6683. (b) Oh, W.; Hwang, Y.-T.; Park, Y. H.; Ree, M.; Chu, S.-H.; Char, K.; Lee, J.-K.; Kim, S. Y. *Polymer* **2003**, *44*, 2519.

(8) Nguyen, C. V.; Carter, K. R.; Hawker, C. J.; Hedrick, J. L.; Jaffe, R. L.; Miller, R. D.; Remenar, J. F.; Rhee, H.-W.; Rice, P. M.; Toney, M. F.; Trollsas, M.; Yoon, D. Y. *Chem. Mater.* **1999**, *11*, 3080.

(9) Hedrick, J. L.; Miller, R. D.; Hawker, C. J.; Carter, K. R.; Volksen, W.; Yoon, D. Y.; Trollsas, M. *Adv. Mater.* **1998**, *10*, 1049.

(10) Nguyen, C.; Hawker, C. J.; Miller, R. D.; Huang, E.; Hedrick, J. L. *Macromolecules* **2000**, *33*, 4281.

(11) (a) Rottman, C.; Grader, G.; DeHazan, Y.; Melchior, S.; Avnir, D. *J. Am. Chem. Soc.* **1999**, *121*, 8533. (b) Dantas de Morais, T.; Chaput, F.; Bailot, J.-P.; Lahlil, K.; Darracq, B.; Levy, Y. *Adv. Mater.* **1999**, *11*, 107.

(12) (a) Lev, O.; Tsionsky, M.; Rabinovich, L.; Glezer, V.; Sampath, S.; Pankratov, I.; Gun, J. *Anal. Chem.* **1995**, *67*, 22A. (b) Harmer, M. A.; Farneth, W. E.; Sun, Q. *J. Am. Chem. Soc.* **1996**, *118*, 7708. (c) Schubert, U. *New J. Chem.* **1994**, *18*, 1049.

(13) (a) Guizard, C.; Lacan, P. *New J. Chem.* **1994**, *18*, 1097. (b) Smaihi, M.; Jermoumi, T.; Marignan, J.; Noble, R. D. *J. Membr. Sci.* **1996**, *116*, 211.

(14) Naudon, A. In *Modern Aspects of Small-Angle Scattering*; Brumberger, H., Ed.; Kluver Academic: Amsterdam, 1995; p 181.

(15) (a) Oh, W.; Shin, T. J.; Ree, M.; Jin, M. Y.; Char, K. *Macromol. Chem. Phys.* **2002**, *203*, 791. (b) Oh, W.; Ree, M. *Langmuir* **2004**, *20*, 6932.

(16) Shin, Y. C.; Choi, K.-Y.; Jin, M. Y.; Hong, S.-K.; Cho, D.; Chang, T.; Ree, M. *Korea Polym. J.* **2001**, *9*, 100.

(17) Bolze, J.; Kim, J.; Huang, J.-Y.; Rah, S.; Youn, H. S.; Lee, B.; Shin, T. J.; Ree, M. *Macromol. Res.* **2002**, *10*, 2.

(18) Oh, W. Ph.D. Thesis, Pohang University of Science & Technology, 2003.

(19) (a) Holy, V.; Pietsch, U.; Baumbach, T. *High-Resolution X-ray Scattering from Thin Films and Multilayers*; Springer-Verlag: Berlin, 1999. (b) Lee, B. Ph.D. Thesis, Pohang University of Science & Technology, Pohang, Korea, 2003. (c) Omote, K.; Ito, Y.; Kawamura, S. *Appl. Phys. Lett.* **2003**, *82*, 544. (d) Lee, B.; Park, Y.-H.; Hwang, Y.-T.; Oh, W.; Yoon, J.; Ree, M. *Nature Mater.* **2005**, *4*, 147.

(20) Rauscher, M.; Salditt, T.; Spohn, H. *Phys. Rev. B* **1995**, *52*, 16855.

(21) Lazzari, R. *J. Appl. Crystallogr.* **2002**, *35*, 406.

(22) Schlomka, J.-P.; Tolan, M.; Schwalowsky, L.; Seeck, O. H.; Stettner, J.; Press, W. *Phys. Rev. B* **1995**, *51*, 2311.

(23) Parratt, L. G. *Phys. Rev.* **1954**, *95*, 359.

(24) (a) Kinning, D. J.; Thomas, E. L. *Macromolecules* **1984**, *17*, 1712. (b) Pedersen, J. S. *J. Appl. Crystallogr.* **1994**, *27*, 595.

(25) (a) Lee, B.; Shin, T. J.; Lee, S. W.; Yoon, J.; Kim, J.; Ree, M. *Macromolecules* **2004**, *37*, 4174. (b) Ruland, W. *J. Appl. Crystallogr.* **1971**, *4*, 70. (c) Koberstein, J. T.; Stein, R. S. *J. Polym. Sci., Polym. Phys. Ed.* **1983**, *21*, 2181.

(26) Balta-Calleja, F. J.; Vonk, C. G. *X-ray Scattering of Polymers*; Elsevier: Amsterdam, 1989.

(27) Young, R. J.; Lovell, P. A. *Introduction to Polymers*, 2nd ed.; Chapman & Hall: London, 1991; Chapter 3.

(28) Huang, Q. R.; Kim, H.-C.; Huang, E.; Mecerreyes, D.; Hedrick, J. L.; Volksen, W.; Frank, C. W.; Miller, R. D. *Macromolecules* **2003**, *36*, 7661.

MA048214E